Proceedings of the 9th International Conference on Physical Modelling in Coastal Engineering (Coastlab24)

Delft, Netherlands, May 13-16, 2024

Conference Paper, DOI: 10.59490/coastlab.2024.686

EXPERIMENTAL STUDY OF IRREGULAR WAVE FIELD WITH MODERATE STEEPNESS AROUND A MONOPILE

IVANDITO HERDAYANDITYA[1,2], MAX STREICHERS[2], EVERT LATAIRE[3] PIETER RAUWOENS[1]

1 Department of Civil Engineering, KU Leuven, Bruges, Belgium, ivandito.herdayanditya@kuleuven.be

2 Department of Civil Engineering, Ghent University, Belgium

3 Maritime Technology Division, Ghent University, Belgium

ABSTRACT

Most offshore wind turbine foundations are of monopile type and need regular marine operations to be conducted nearby during the lifetime of the turbine. Proper wave estimation around the monopile is needed to assure the safety of the operations. The trend of increasing monopile's diameter also adds the need to investigate the wave field around the increased monopile diameter for the marine operation analysis. Experimental campaigns of wave field around a monopile in irregular incident waves with different steepness are reported in this study to extend the available experiments which focused mostly on the runup of cylindrical structures. The wave field at two radial positions and six angular positions around the monopile is investigated. The results are processed to obtain the Linear Transfer Function of the wave field around the monopile and the Exceedance Probability of the wave height and crest of the waves around the monopile. For the tested conditions, the linear solution accurately captures the frequency domain characteristics and the exceedance probability of wave height but fails to predict the crest exceedance probability.

KEYWORDS: Monopile, Wave Field, Linear Transfer Function, Exceedance Probability

1 INTRODUCTION

Affordable and Clean Energy is one of the Sustainable Development Goals (Goal 7) which has been proposed to protect the planet and improve the life quality of human beings (UN, 2015). Offshore wind energy is one of renewable energies that has grown substantially in the last years (GWEC, 2023). There are various structure types that are utilised to place wind turbines in the offshore environments, such as monopiles, jackets, and gravity-based foundations, where monopiles have become the most built offshore wind support structure. Furthermore, the diameter of monopiles has also increased substantially to extend its capability to be installed in the intermediate water depth.

Estimation of the wave field around a monopile (WFAM) is needed to assess safe marine operations. An analytical solution to estimate WFAM has been proposed by MacCammy and Fuchs (1954) which is based on linear potential flow. However, some regular wave experiments have shown that the linear potential flow solution underestimates the runup of the monopile (Kriebel, 1992; Morris-Thomas and Thiagarajan, 2004). A nonlinear analytical solution is also available (Kriebel, 1990; Chau and Taylor, 1992; Molin 1995) which improves the estimation of the WFAM. Further, the regular wave solution is explored to compute the irregular WFAM. The linear potential flow solution was employed by Niedzwecki and Duggal (1992) to predict the wave spectrum at several runup position by means of Linear Transfer Function from regular wave linear potential flow solutions. The analytical solution of nonlinear irregular wave field was also applied by Wang and Low (2019) which found that nonlinearity has a negligible effect on the spectral analysis but is important for extreme value estimation.

Numerical tools are also utilised to compute the WFAM. Linear Potential Flow solvers (e.g. Capytaine (Ancellin and Dias, 2019; Babarit and Delhommeau, 2015) is capable to estimate the linearized WFAM. It relies on the green function solutions of linearized boundary conditions. Simulations of potential flow tank has also been employed to capture the nonlinear WFAM (Ferrant *et al.*, 1999; Büchmann *et al.*, 1999; Lin *et al.*, 2021). Furthermore, Computer Fluid Dynamics (CFD) tools have been utilized to capture the runup around the monopile. Herdayanditya *et al.* (2022) employed CFD to estimate the runup around a monopile and found a good agreement compared to the experiments. Due to the capability to explore turbulence effect in the CFD, the runup around monopile within breaking wave conditions is also studied with CFD tools (Liu *et al.*, 2019). However, it should be noted that high fidelity numerical tools like CFD might not be suitable for marine operational needs where computational cost remains an issue.

Empirical models are also widely used to estimate the maximum wave runup (ζ_C) around a monopile. The α and β are the empirical constants in Eq. (1) which give empirical relationship between the wave height H_W, water velocity u, and the gravity acceleration g. Hallermeier (1976) estimated the maximum runup with the help of Bernoulli equation at the stagnation point where α and β in Eq. (1) are equal to one. Further, Eq. (1) is improved empirically from set of experiments to tune the α and β (Niedzwecki and Duggal, 1992). De Vos *et al.* (2007) improved the Eq. (1) by applying second order theory to estimate the velocity rather than with the airy theory, which then new empirical coefficients of α and β are found. Further, Andersen *et al.* (2011) applied stream function to estimate the velocity and split the coefficients into low and high steepness cases. This approach also gives a satisfactory result of wave runups in breaking wave conditions (Ramirez *et al.*, 2013). These empirical approaches focus on the runup practical estimation which do not give information of WFAM.

$$\zeta_C = \alpha H_w + \beta \frac{u^2}{2g} \tag{1}$$

This research focuses on investigation of WFAM due to moderate steepness of incident irregular waves. The characteristics of WFAM are sought so that marine operation analysis can be performed with proper assumptions. Section 2 provides the theoretical background needed to post process the data. It contains analytical solution of wave field around monopile, signal processing tool to extract linear transfer function, and time series analysis method. Afterwards, in Section 3, the physical experiment cases and procedures are given. The results of the experiments are provided and discussed in Section 4. Finally, the conclusion is drawn up in Section 5.

2 WAVE FIELD AROUND A MONOPILE (WFAM)

2.1 Linear Potential Theory

The water motion around the monopile can be seen as potential flow under the assumption of inviscid, irrotational, and incompressible fluid. After linearization of the free surface, the WFAM amplitude (ζ_o) around the monopile with radius (R) at a radial position (r) and an angular position (θ) can be computed with Eq. (2) (MacCamy and Fuchs, 1954; Kriebel, 1990). The H_W is the incident wave height, $\epsilon_n = 1$ if $n = 0$; else $\epsilon_n = 2\, i^{-n}$, $J_n(kr)$ is the Bessel function of the first kind, and $H_n(kr)$ is the Henkel function. The Bessel and Henkel functions are function of the radial position and the wave number (k). Moreover, the time series of the WFAM is constructed as $\zeta(r,\theta,t) = \mathbb{R}\{\zeta_o(r,\theta)\exp(-\omega t + \phi_\zeta)\}$, where the t is the time, ω is the wave angular frequency, and ϕ_ζ is the phase of the WFAM. It has to be noted that the linearized WFAM also assumes linear incident waves where the time series of the water elevation is $\eta(x,y,t) = \mathbb{R}\left\{\frac{H_W}{2}\exp[i(kx\cos\psi + ky\sin\psi)]\exp\left[i\left(-\omega t + \phi_\eta\right)\right]\right\}$ at x, y cartesian position with one wave direction (ψ).

$$\zeta_o(r,\theta) = \frac{H_W}{2}\sum_{n=0}^{\infty}\epsilon_n\left[J_n(kr) - \frac{J_n'(kR)}{H_n'(kR)}H_n(kr)\right]\cos(n\theta) \tag{2}$$

2.2 Linear Transfer Function

$$\mathrm{LTF}(r,\theta) = \frac{H_\zeta}{H_W} = \frac{2\zeta_o(r,\theta)}{H_W} \tag{3}$$

Linear Transfer function (LTF) is defined as the ratio between the WFAM height (H_ζ) and the incident wave height (H_W). The LTF is checked to characterise the WFAM in the frequency domain. It is equivalent to the seakeeping terminology of Response Amplitude Operator (RAO) where it transforms the incident waves into motion responses. In this study LTF is characterisation of the WFAM due to incident waves

The theoretical LTF is defined as Eq. (3) where the $\zeta_o(r,\theta)$ is computed from Eq. (2). Spectral analysis is needed to extract the LTF in the irregular wave experiments. It employs the Fast Fourier Transform (FFT) where it transforms the input $p(t)$ and output $q(t)$ time series into the FFT's amplitude input and output, $P(f)$ and $Q(f)$ respectively. Afterwards, the LTF can be computed with Eq. (4) where $E[PQ^*]$ refers to the cross density spectral of the input and output signal and $\mathrm{E}[|P|^2]$ refers to the density spectral input. The WFAM LTF computation in irregular waves is performed by taking the incoming waves as the input signal, $p = \eta(x,y,t)$, and the WFAM as the output signal, $q = \zeta(r,\theta,t)$. Furthermore, Welch method (Welch, 1967) is applied to obtain the density spectrum.

$$\mathrm{LTF} = \frac{\mathrm{E}[PQ^*]}{\mathrm{E}[|P|^2]} \tag{4}$$

The LTF computation in Eq. (4) assumes that the input and the output are related linearly. The linear relationship can be identified by the linear coherence between the input and the output signal system. The coherence is computed as in Eq. (5) where the value of coherence is $0 \le C \le 1$. The unity coherence refers to system which is fully linear between the input and the output.

$$\text{Coh.} = \frac{\mathrm{E}[(PQ)^2]}{\mathrm{E}[|P|^2]\mathrm{E}[|Q|^2]} \tag{5}$$

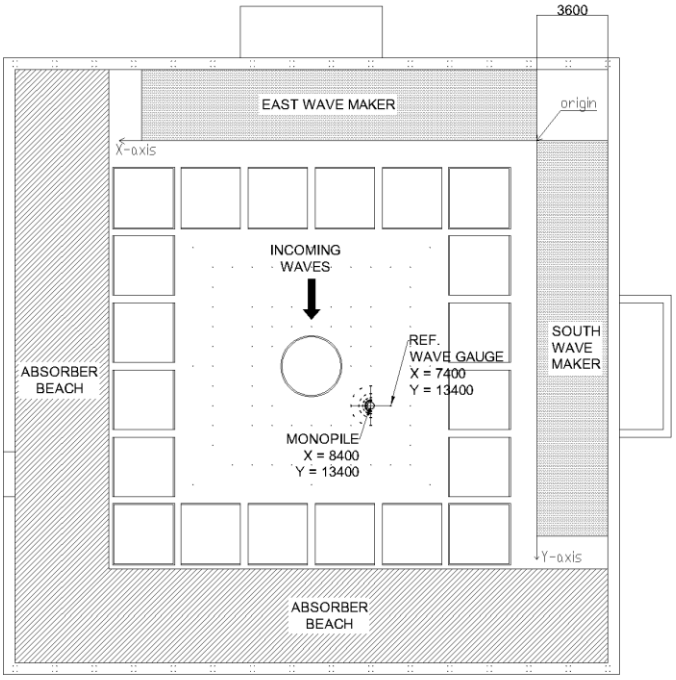

Figure 1. Drawing scheme for the monopile location inside the wave tank along with the wave makers and wave absorber beaches.

Table 1. Target irregular wave parameters for the experimental campaign

	Model		Full Scale	
	T_p (s)	H_s (s)	T_p (s)	H_s (s)
Wave 1	1.67	0.10	8.34	2.51
Wave 2	1.67	0.13	8.34	3.35
Wave 3	1.67	0.20	8.34	5.02

Table 2. The nondimensional wave parameters of the wave and monopile for the experiments

	Steepness	Dispersity	Diffraction Number
	$\frac{1}{2}k_\mathrm{p}H_\mathrm{s}$	$k_\mathrm{p}h$	$k_\mathrm{p}R$
Wave 1	0.075	2.09	0.30
Wave 2	0.10	2.09	0.30
Wave 3	0.15	2.09	0.30

2.3 Probability of Exceedance

$$F_p(x_p) = 1 - \mathrm{e}^{-\frac{x_p^2}{8m_o}} \tag{6}$$

$$S_\zeta(f) = \mathrm{LTF}^2\, S_\eta(f) \tag{7}$$

The Exceedance Probability is taken to characterize the WFAM time domain. Zero up-crossing definition is used to identify the WFAM components in the time series measurement. Within each up-crossing wave component, i, the maximum (ζ_{C_i}) and the minimum (ζ_{T_i}) elevations are measured and recorded. The difference between the ζ_{C_i} and ζ_{T_i} is identified as wave height ($H_{\zeta_i} = 2\zeta_{o_i}$). The wave height and wave crest Cumulative Distribution Function (CDF), $F_H(x_p)$ and $F_{2\eta_\mathrm{C}}(x_p)$ respectively, can subsequently be constructed. The CDF defines the probability of occurrence when the wave parameter (x) is

between 0 and a specified threshold (x_p), i.e. $F(x_p) = \Pr(x \leq x_p)$. In this study the theoretical wave crests ($x_p = 2x_{\eta c}$) and wave height parameters ($x_p = H$) are computed according to the Rayleigh distribution as in Eq. (6) where the m_o is the zeroth moment of the WFAM spectrum. It is based on the assumption of the linearized random waves theory, where the wave components in different frequencies are superimposed on each others. The WFAM spectrum (S_ζ) is computed according to Eq. (7) (Niedzwecki and Duggal, 1992), where the S_η is the incident wave spectral and LTF is computed according to JONSWAP Spectrum. Afterwards, probability of exceedance (P_E) is computed according to Eq. (8). The exceedance probability describes the probability of occurrence when the wave parameter is above the specified threshold i.e. $F(x_p) = \Pr(x > x_p)$.

$$P_E(x_\mathrm{p}) = 1 - F_p(x_p) \tag{8}$$

3 EXPERIMENT SET-UP

The experiment was conducted in the Coastal & Ocean Basin (COB) in Ostend, Belgium. The wave tank dimension is 30m x 30m with 20m x 20m L-shaped wave makers and absorbing beaches on the other two sides (Figure 1). The wave makers are also capable of performing active absorption. A monopile was placed at a position where the waves have developed (e.g. no influence of the evanescence waves). It was concluded from a series of regular wave tests without the monopile in place to verify the wave development by checking its spatial variation. During the test, only East wave maker was activated to generate the waves while the South wave maker only acted as an active wave absorber and a guide wall.

Table 3. The measured T_p and H_s and the relative difference to the target

	T_p (s)	diff. (%)	H_s (s)	diff. (%)
Wave 1	1.707	2.40	0.101	2.51
Wave 1	1.707	2.40	0.136	3.35
Wave 1	1.707	2.40	0.198	5.02

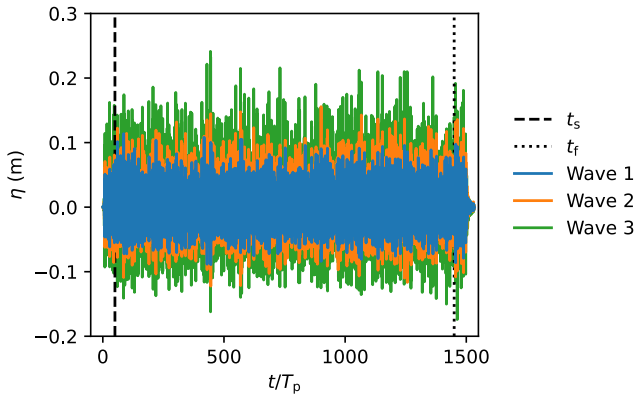

a. The time series record of the incident waves measured at the reference wave gauge without monopile in place

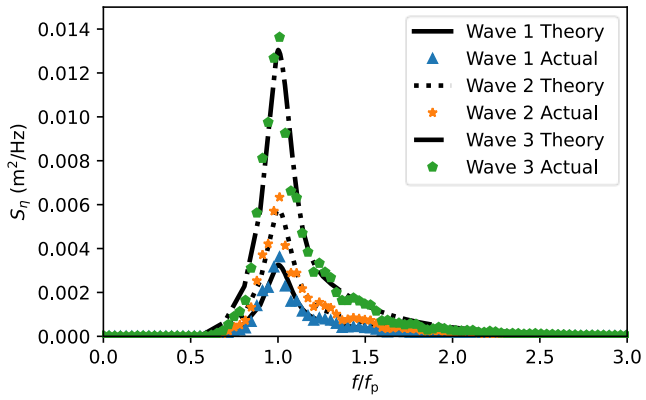

b. Comparison of actual wave spectra to the theoretical wave spectra in all wave cases with Jonswap Spectrum $\gamma = 3.3$

Figure 2. Time series and wave spectra of the incident waves

3.2 Test Cases

A monopile with 10 m diameter, expected for 15 MW wind turbine, was taken as the monopile reference (Gaertner *et al.*, 2020). The experiment study was with 1:25 Froude length scale, hence the diameter of the model was 0.4 m. The water depth for the experiments was 1.4 m which mimicked the 35 m water depth. Three long crested irregular waves were generated with the same peak period T_p but varying steepness k_pH_s. Table 1 shows the model and the full scale wave cases along with the wave parameters, identified by Wave 1, Wave 2, and Wave 3. Furthermore, Table 2 describes the nondimensional parameters of the cases, namely the steepness, dispersity, and the diffraction number. The steepness of the cases is within the moderate steepness range to capture the nonlinearity of operational conditions. The dispersion suggests that the experiments were in the moderate water depth, while the diffraction number indicates small effect of diffraction force. Although the diffraction number is small, disturbance of the waves is expected to be observed around the monopile, as seen in the nonlinear regular waves runup (Kriebel, 1995). All the irregular waves were generated with JONSWAP wave model where uniform peak enhancement factor of 3.3 was applied.

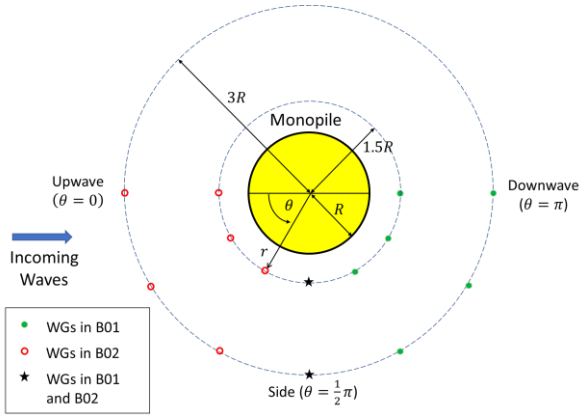

(a) Resistance WGs layout in B01 and B02. The position reference is according to the center of the monopile with r represents the radial position and the θ represents angular position

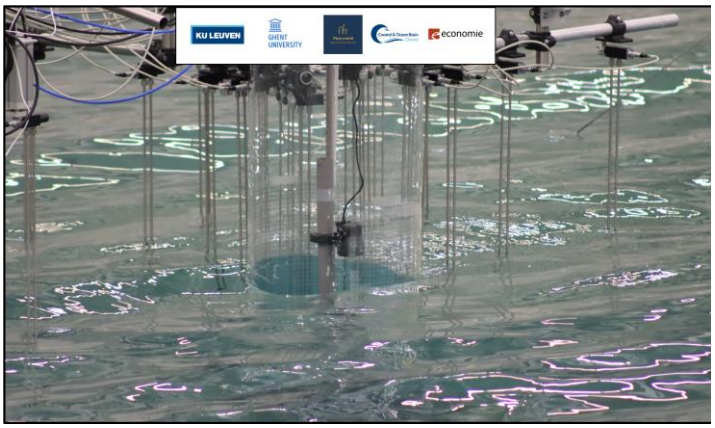

(b) Actual Condition of resistance WGs and the monopile in B01

Figure 3. Wave gauge arrangement in the experiment to monitor the WFAM

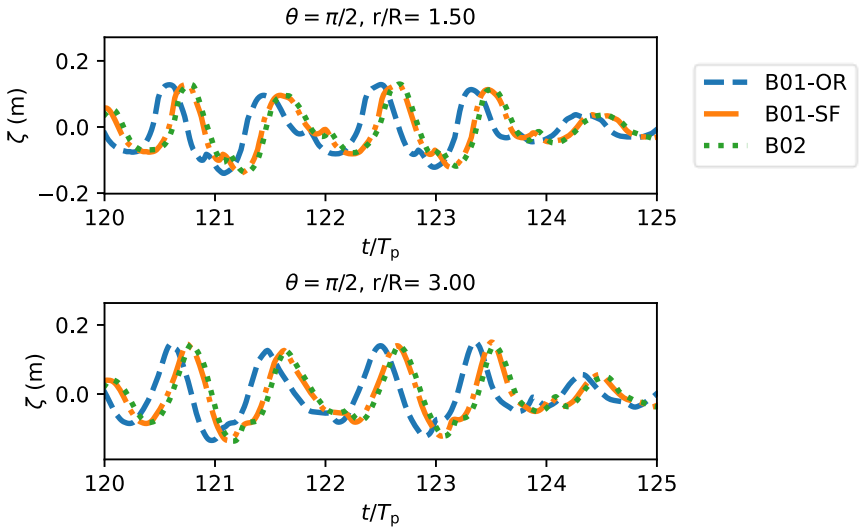

Figure 4. Comparison of the WFAM measurements for runs of the same time series (Wave 3) featuring two different WGs layout (B01 and B02)

3.3 Procedure

The experimental campaign began with tuning the irregular wave measurement with B00 arrangement. The B00 used one reference wave gauge (WG) located at the side of the monopile as seen in Figure 1. This was performed to assure that the

actual waves in the basin were as the target waves in Table 1. The head and the tail of the time series are cut for the analysis at the starting time, $t_s = 50\,T_p$ and finishing time, $t_f = 1450\,T_p$ (Figure 2a). This gives a total period of $1400T_p$ laboratory scale simulation which is 3.2 hours full scale simulation. Figure 2 shows the incident wave time series and wave spectra in the basin as compared to the theoretical spectra. The spectra are obtained with Welch method where the time series are split into segments, consisting of 2048 data. Overlapping of 50% data segments is taken for the analysis. The statistical parameters obtained from the measured spectrum are shown in Table 3 where a good agreement between the actual waves and the target waves was achieved.

The reference WG and the monopile were installed side by side with additional WGs of two different wave probe arrangements namely B01 and B02 (Figure 3a). The B01 was at first used to simulate the wave cases in Table 1. Subsequently, it was rotated into B02 to simulate again the same wave cases, while keeping two WGs (star symbol in Figure 3a) at the same locations. The WGs are resistance WGs with measurement frequency of 40 Hz. $\theta = 0$ is at the upwave side of the monopile while $r = 0$ is at the center of the monopile. The B01 and B02 WGs recorded the wave field around the monopile at two radial positions $r = [1.5R, 3R]$ and seven angular positions $\theta = [0, \frac{1}{6}\pi, \frac{1}{3}\pi, \frac{1}{2}\pi, \frac{2}{3}\pi, \frac{5}{6}\pi, \pi]$.

Comparison of the wave WG between B01 and B02 in the Wave 3 at $\theta = \frac{1}{2}\pi$ are shown in Figure 4. It shows a slight shift of ≈ 0.25 s, as seen from comparison between B01-OR and B02. To account for the shift, the time series of the WFAM of B01 is shifted accordingly so that the B01-SF is now identical to the B02. The shifting also appears at the Wave 1, Wave 2, and Wave 3, and the treatment is applied similarly. Nevertheless, the shifting of the time series will not affect the spectra analysis because the spectral analysis utilizes only the recorded elevation and the frequency measurement.

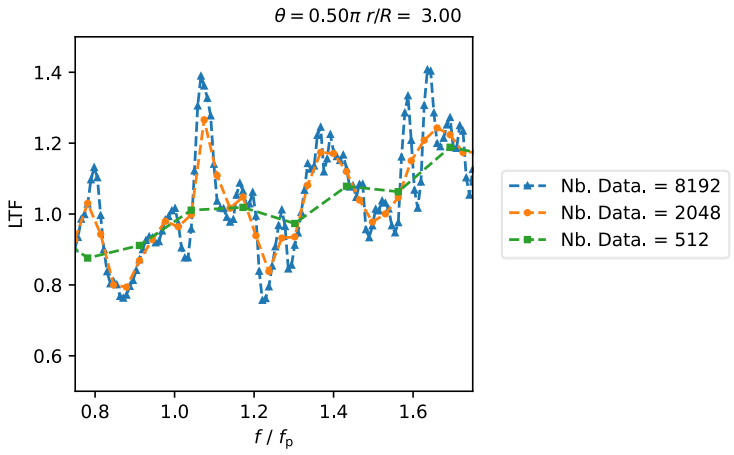

Figure 5. Frequency leakage of LTF computation at high number of data in one segment

4 RESULTS AND DISCUSSION

4.1 Transfer Function

The incident waves and WFAM records are utilized to obtain the LTF at the angular and radial positions. It is computed according to Eq. (4). Beside the LTF, coherence is also investigated (Eq. 5) to check if the linear relationship occurs between the incident waves and the WFAM. The LTF obtained from the experiments are also compared to the theoretical LTF (Eq. 3). The LTF computation is with 512 data in each segment, lower than 2048 data as used in Figure 2b. It is because the frequency leakage of other frequencies appears in the LTF computation. It is demonstrated by the measurement at the side of the monopile $\left(r = 3.0R,\ \theta = \frac{\pi}{2}\right)$ where the LTF is shown in Figure 5. It is seen that with higher number of data at each segment, Welch method loses its capability to smoothen the LTF estimation. With more data in each segment, the oscillation of the LTF at the frequency domain is more apparent. However, with lower number of data in each segments, the frequency resolution will become less, thus missing information of the frequency domain. Therefore, to capture enough frequencies and not having numerical problems, 512 data in each segment are taken for the analysis.

Figure 6 shows the LTF of the experiment and the theoretical estimation from one location at the upwave side ($\theta = 0, r = 1.5R$). The analysis can be split into three regions: 1. low frequency area ($f/f_p < 0.75$), 2. wave frequency input ($0.75 < f/f_p < 1.75$), 3. high frequency ($f/f_p > 1.75$). The splits are according to the magnitude of the coherence. Coherance that is close to unity is observed in the wave frequency where substantial wave energy occurs i.e., the second region. The coherence is small on the other two sides, the low frequency and high frequency areas. It indicates that the WFAM and incident waves of these frequency components are related nonlinearly in the both frequency ranges. The nonlinearity

comes from the higher order components of the monopile diffraction interaction which is also seen in the regular wave-monopile interaction (Kriebel, 1992). It is also possible that the wave-wave interactions either in the sum frequencies (impacting the high frequency region) or difference frequencies (impacting low frequency region) also play a role in the nonlinearity relationship. To confirm this, bichromatic wave study shall be conducted.

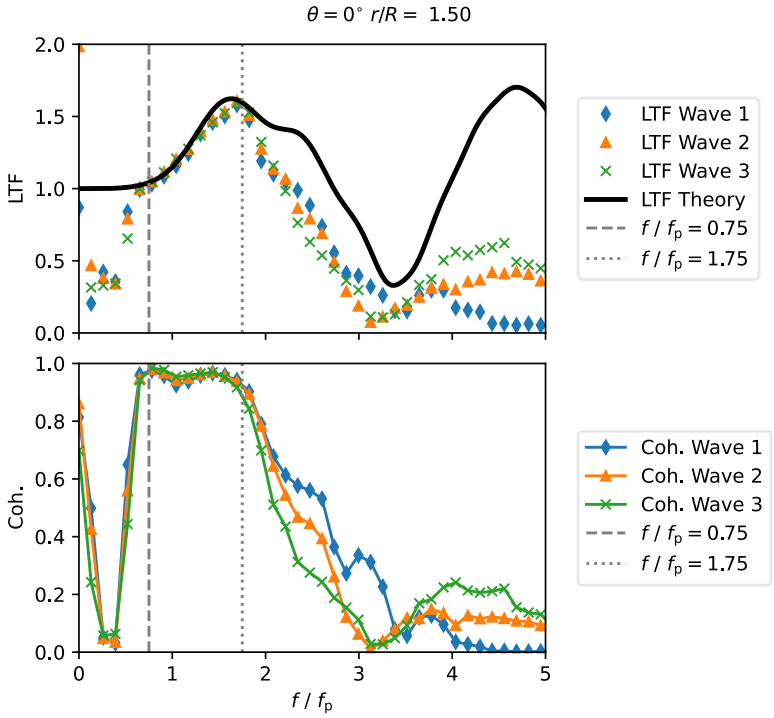

Figure 6. The LTF results of the point at the upwave $\boldsymbol{\theta = 0, r = 1.5R}$

The monopile in the low frequency waves (hence: long waves) under the linear potential flow theory behaves as transparent structures (LTF =1). However, the LTF of the experiments in this study does not agree with the theoretical LTF. The coherence is also low in this region, thus indicating nonlinear relationship of the incident waves and the WFAM. The wave energy input in the low frequency area is small (Figure 2b) but some wave components appear in the WFAM and not caused by linear relationship between the input and output. The response that appears in the WFAM is most probably due to the interaction between difference frequencies. Special discussion is given at the $f/f_p = 0$ where the LTF is also not collapsing at unity (as the theoretical LTF). This represents the change of the mean value between the incident waves and the WFAM. This phenomenon is known as the set-up or the set-down of the WFAM. In the regular waves it is observed and Kriebel (1990) derived that the value comes from the square of the potential of the first order solution.

In the wave frequency input region, linear relationship between the wave input and wave field around the monopile can be concluded because the coherence in this region is higher than 0.85. Furthermore, the LTF estimation from the experiments collides well with the estimation of the linear potential flow region. Increasing wave steepness also does not seem to change the linear relationship in this region. This is in line with the previous findings (Niedzwecki and Duggal 1992; Wang and Low 2019) where the spectral of the wave field around the monopile is shown to be indifferent between the linear and nonlinear cases.

The oscillation of the theoretical LTF at the high frequency can be explained by the standing waves formed from incident waves and the diffracted waves at this location. Further, in the high frequency regions, the interaction between the incident waves and WFAM are nonlinear as seen from the low coherence value. Therefore, the LTF from the experiment does not give the same LTF as the theoretical waves. In the high frequency regions, the different incident wave steepness appears to also give different coherences where the low steepness case gives higher wave coherence than the high steepness of incident waves.

4.2 Exceedance Probability

The P_E of the wave height and the crest at the upwave location and one radial position are shown in Figure 7. The figures are with the Wave 3 which is the most nonlinear incident waves being investigated in this paper. The P_E of the incident waves and the WFAM are shown in two styles: 1. The P_E is with linear scale (left side) and 2. The P_E is with logarithmic scale (right side). The logarithmic scale is utilized to zoom in the extreme condition where the Exceedance Probability is very low while the high Exceedance Probability is more visible in the linear scale.

The P_E of the incident waves and the WFAM from the Wave 3 are also compared to the Rayleigh P_E which is computed from the Rayleigh CDF of the incident or the WFAM with Eq. (6) and Eq. (8). In order to compute the Rayleigh CDF, the zeroth moment (m_o) is needed in which for the incident waves it can be obtained from the JONSWAP spectrum while for the WFAM it can be obtained from the spectrum of Eq. (7).

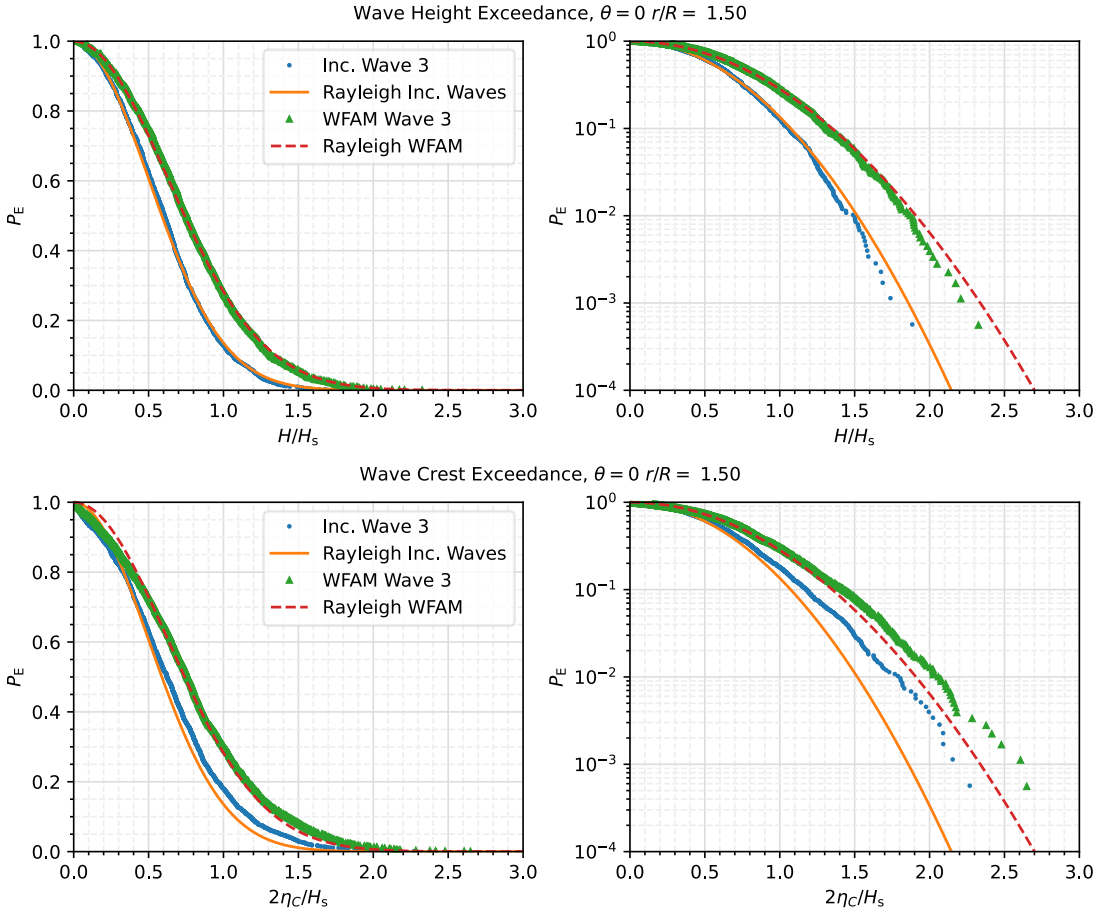

Figure 7. The Exceedance Probability of the wave height and the wave crest of incident waves and WFAM in Wave 3 at $\theta = 0$ and $r = 1.5R$

The Rayleigh WFAM height and crest P_E in Figure 7 are higher than the incident wave Rayleigh because at this location the LTF is higher than unity at the wave frequency region (Figure 6). It is also as what is observed from the experiment, although the agreement between the experiment and the Rayleigh estimation accuracy differs between the wave height P_E and crest P_E. The agreement with respect to the wave height is decent both at the low and the high P_E as shown from the linear and logarithmic P_E. However, the performance of Rayleigh distribution in estimating the crests events is not as decent as in estimating the wave height. In the high exceedance probability region (low crest events), it performs well although minor discrepancy is noticed at the very high exceedance probability wave crest events ($P_E \approx 0.8 - 1.0$). On the other hand, in the low exceedance probability region (high crest events), significant underestimation of Rayleigh P_E is observed. The underestimation of the crests is known in nonlinear runup of the regular waves (Herdayanditya, 2023) when the results are compared to the linear wave runup theory. It is also observed in the irregular waves condition of the WFAM from this experiment. Furthermore, the underestimation of crest P_E is also seen in the incident waves.

Overview of the P_E of the wave height and the wave crest at different locations around the monopile are given in Figure 8 and Figure 9. Three angular locations are taken which are: 1. $\theta = 0$, upwave location, to represent the standing wave interaction between the incident and the diffracted waves, 2. $\theta = \frac{2}{3}\pi$, to represent the most nonlinear region of the interaction between the incident waves and the diffracted waves, 3. $\theta = \pi$, to represent the shielding area. The first radial position ($r = 1.5R$) is shown in Figure 8 while the second radial position ($r = 3R$) is shown in Figure 9. In both of the figures the wave height and crest P_E from the Wave 1, Wave 2, Wave 3 and Rayleigh distribution are shown.

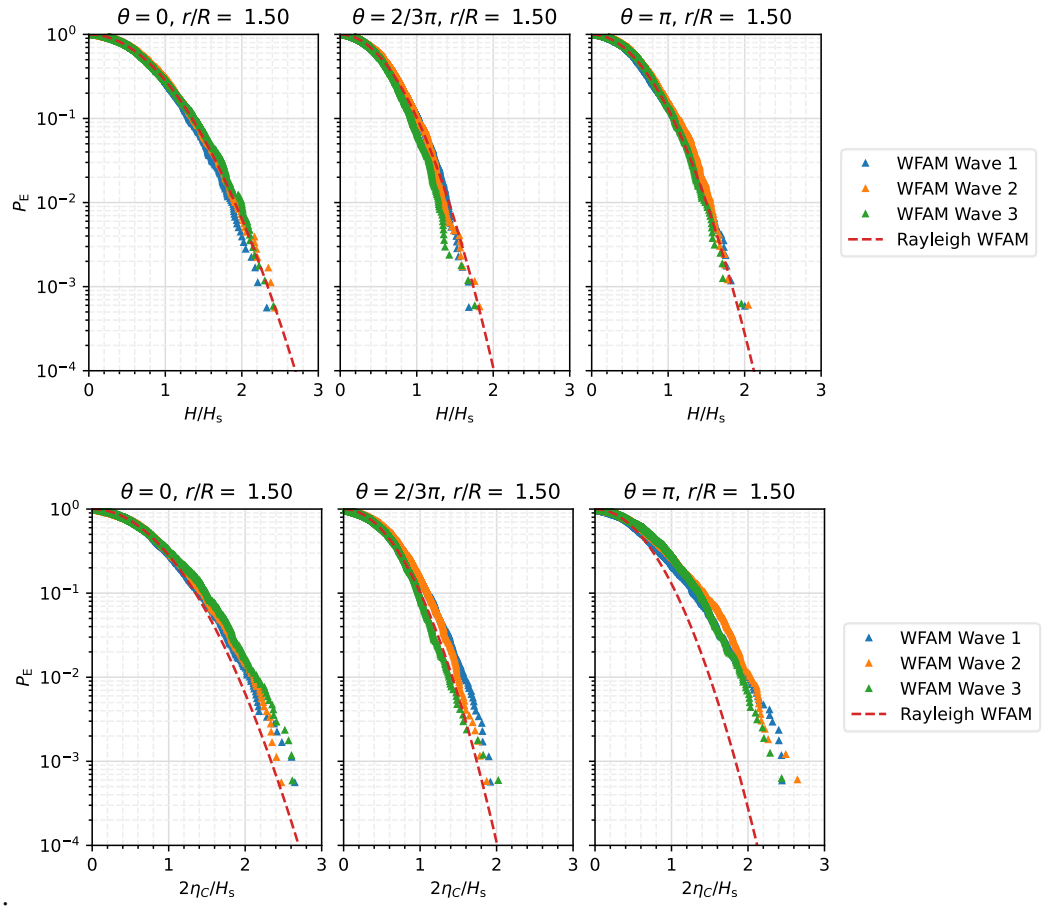

Figure 8. The Exceedance Probability of the wave height and the wave crest at various angular position at $r = 1.5R$

In both radial locations and the angular locations, the agreement of Rayleigh distribution to the wave height estimation is satisfactory but the crests. The crest disagreement appears to also depend on the wave steepness of the incident waves. At the upwave location, the higher the incident wave steepness, the bigger the discrepancy of the crest P_E at the high wave high event to the Rayleigh P_E. However, it does not seem to apply in other angular positions at both radial positions. At the $\theta = 2/3\pi$, the wave crest P_E from the highest steepness wave height is the lowest P_E. However, the trend changes at the $r = 3.0R$. It is expected due to the effect of nonlinearity is still high at location close to the monopile which gives a sharper through instead of sharper crest as noticed from Wang and Low (2019).

In the engineering perspective, Figure 8 and Figure 9 give evidence that if the wave height becomes the main interest in the limiting factor of the marine operations, random waves with Rayleigh distribution can be used, thus linear wave theory is sufficient. The WFAM spectrum can also be computed with linear theory as in Eq. (7). However, if the crest becomes the main interest of the operation limitation, linear theory is not sufficient.

5 Conclusion

The wave field around a monopile (WFAM) shall be estimated accurately in order to increase the safety and efficiency of marine operations near monopiles. Experiments of the WFAM were performed to investigate the behaviour of irregular WFAM. The incident irregular waves were initially verified against the theoretical waves to assure that the measured wave field in the tank was as the target waves. Wave gauge rotations techniques to capture more angular and radial positions with limited wave gauges are verified by comparing the WFAM measurements at the same locations within two arrangements under two identical test cases that were performed separately. The repeatability was considered good to assume that the two experiments are one identical experiment. Besides, the slight shift of the phase does not seem to affect analysis. Two analyses are provided in this study which are the LTF and the Exceedance Probability of the waves. The two analyses are to represent the frequency domain and time series characteristics of the wave field respectively. In the frequency domain, the Linear Transfer Function (LTF) of the wave field at different measurement positions are compared to the theoretical LTF. The LTFs that are extracted from experiments appear to agree well with the theoretical LTF in the wave input frequency regions. On the low and high frequency regions with much smaller incident wave density, it is driven by nonlinear behaviour considering the coherence between the incident waves and the WFAM being low. The Exceedance Probability of the wave height and crests

are investigated. It is found that the wave height can be estimated with Rayleigh distribution but the crests. Depending on the sensitivity needs of the marine operations, linear model can be a powerful model to estimate the wave field around monopile. In case where energy of the waves is the point of interest (e.g. installation process of scour protection or crew transfer operations), the amplitude will be more important than the crest estimation. On the other hand, for operations that require proper crest estimation (e.g. dry area estimation), linear model shall be corrected.

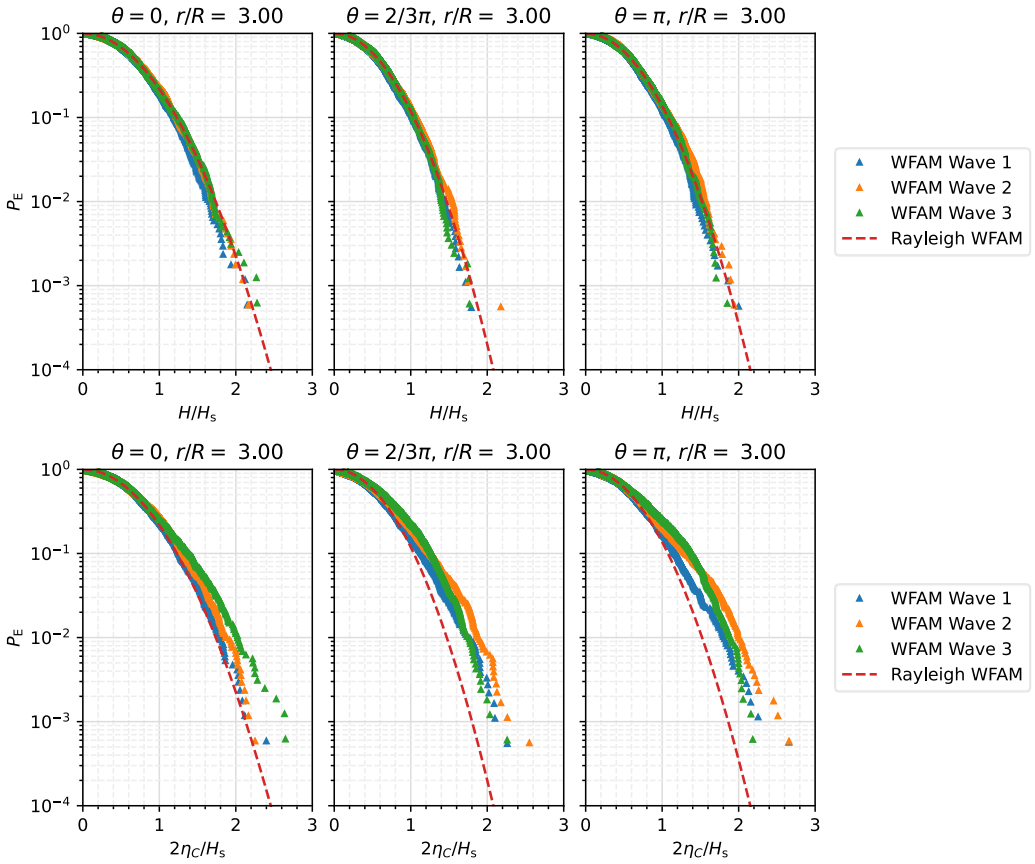

Figure 9. The Exceedance Probability of the wave height and the wave crest at various angular position at $r = 3R$

ACKNOWLEDGEMENT

This research is supported by the Energy Transition Fund (ETF), PhairywinD Project. An appreciation is also given to the Coastal & Ocean Basin team to facilitate the experiments.

REFERENCES

Ancellin, M. and Dias, F., 2019. Capytaine: a Python-based linear potential flow solver. Journal of Open Source Software, 4(36), p.1341.

Andersen, T.L., Frigaard, P., Damsgaard, M.L. and De Vos, L., 2011. Wave run-up on slender piles in design conditions—Model tests and design rules for offshore wind. Coastal Engineering, 58(4), pp.281-289.

Babarit, A. and Delhommeau, G., 2015, September. Theoretical and numerical aspects of the open source BEM solver NEMOH. In 11th European wave and tidal energy conference (EWTEC2015).

Büchmann, B., Skourup, J. and Kriebel, D.L., 1999. Second order wave interaction with a large structure. In Coastal Engineering 1998 (pp. 1613-1624).

Chau, F.P. and Taylor, R.E., 1992. Second-order wave diffraction by a vertical cylinder. Journal of Fluid Mechanics, 240, pp.571-599.

De Vos, L., Frigaard, P. and De Rouck, J., 2007. Wave run-up on cylindrical and cone shaped foundations for offshore wind turbines. Coastal Engineering, 54(1), pp.17-29.

Ferrant, P., Malenica, S. and Molin, B., 1999. Nonlinear wave loads and runup on a vertical cylinder. ADVANCES IN FLUID MECHANICS, 24, pp.101-136.

Gaertner, E., Rinker, J., Sethuraman, L., Zahle, F., Anderson, B., Barter, G.E., Abbas, N.J., Meng, F., Bortolotti, P., Skrzypinski, W. and Scott, G.N., 2020. IEA wind TCP task 37: definition of the IEA 15-megawatt offshore reference wind turbine (No. NREL/TP-5000-75698). National Renewable Energy Lab.(NREL), Golden, CO (United States).

GWEC, G. W. E., 2023. Global wind report 2023.

Hallermeier, R.J., 1976. Nonlinear flow of wave crests past a thin pile. Journal of the Waterways, Harbors and Coastal Engineering Division, 102(4), pp.365-377.

Herdayanditya, I., Rauwoens, P., Fernandez, G.V., Martínez-Estévez, I. and Lataire, E., 2022. Monopile run-up study using Eulerian and Lagrangian numerical models. Trends in Renewable Energies Offshore, pp.491-499.

Kriebel, D.L., 1990. Nonlinear wave interaction with a vertical circular cylinder. Part I: Diffraction theory. Ocean Engineering, 17(4), pp.345-377.

Kriebel, D.L., 1992. Nonlinear wave interaction with a vertical circular cylinder. Part II: Wave run-up. Ocean engineering, 19(1), pp.75-99.

Lin, Z., Qian, L., Bai, W., Ma, Z., Chen, H., Zhou, J.G. and Gu, H., 2021. A finite volume based fully nonlinear potential flow model for water wave problems. Applied Ocean Research, 106, p.102445.

Liu, S., Gatin, I., Obhrai, C., Ong, M.C. and Jasak, H., 2019. CFD simulations of violent breaking wave impacts on a vertical wall using a two-phase compressible solver. Coastal Engineering, 154, p.103564.

MacCamy, R.C. and Fuchs, R.A., 1954. Wave forces on piles: a diffraction theory (No. 69). US Beach Erosion Board.

Molin, B., 1995. Third-harmonic wave diffraction by a vertical cylinder. Journal of Fluid Mechanics, 302, pp.203-229.

Morris-Thomas, M.T. and Thiagarajan, K.P., 2004. The run-up on a cylinder in progressive surface gravity waves: harmonic components. Applied Ocean Research, 26(3-4), pp.98-113.

Niedzwecki, J.M. and Duggal, A.S., 1992. Wave runup and forces on cylinders in regular and random waves. Journal of waterway, port, coastal, and ocean engineering, 118(6), pp.615-634.

Niedzwecki, J.M. and Duggal, A.S., 1992. Wave runup and forces on cylinders in regular and random waves. Journal of waterway, port, coastal, and ocean engineering, 118(6), pp.615-634.

Ramirez, J., Frigaard, P., Andersen, T.L. and de Vos, L., 2013. Large scale model test investigation on wave run-up in irregular waves at slender piles. Coastal Engineering, 72, pp.69-79.

UN, 2015. Transforming our world: the 2030 agenda for sustainable development. UN Doc. A/RES/70/1 (September 25, 2015).

Wang, Z. and Low, Y.M., 2019. Analysis of the extreme wave elevation due to second-order diffraction around a vertical cylinder. Applied Ocean Research, 86, pp.222-238.

Welch, P., 1967. The use of fast Fourier transform for the estimation of power spectra: a method based on time averaging over short, modified periodograms. IEEE Transactions on audio and electroacoustics, 15(2), pp.70-73.